RSC Advances

PAPER

View Article Online
View Journal | View Issue

Cite this: *RSC Adv.*, 2024, **14**, 10120

Synergistic effects of a copper–cobalt–nitroisophthalic acid/neodymium oxide composite on the electrochemical performance of hybrid supercapacitors

Asma Khizar,[a] Muhammad Zahir Iqbal,*[a] Ayesha Zakir,[a] Misbah Shaheen,[a] Saikh Mohammad Wabaidur[b] and Mian Muhammad Faisal[c]

Received 5th March 2024
Accepted 13th March 2024

DOI: 10.1039/d4ra01719f

rsc.li/rsc-advances

Hybrid supercapacitors can produce extraordinary advances in specific power and energy to display better electrochemical performance and better cyclic stability. Amalgamating metal oxides with metal–organic frameworks endows the prepared composites with unique properties and advantageous possibilities for enhancing the electrochemical capabilities. The present study focused on the synergistic effects of the CuCo(5-NIPA)–Nd_2O_3 composite. Employing a half-cell configuration, we conducted a comprehensive electrochemical analysis of CuCo(5-NIPA), Nd_2O_3, and their composite. Owing to the best performance of the composite, the hybrid device prepared from CuCo(5-NIPA)–Nd_2O_3 and activated carbon demonstrated a specific capacity of 467.5 C g^{-1} at a scan rate of 3 mV s^{-1}, as well as a phenomenal energy and power density of 109.68 W h kg^{-1} and 4507 W kg^{-1}, respectively. Afterwards, semi-empirical techniques and models were used to investigate the capacitive and diffusive mechanisms, providing important insights into the unique properties of battery–supercapacitor hybrids. These findings highlight the enhanced performance of the CuCo(5-NIPA)–Nd_2O_3 composite, establishing it as a unique and intriguing candidate for applications requiring the merging of battery and supercapacitor technologies.

1. Introduction

The rapid development of electronic technology has spurred an increasing demand for energy-storage devices. This spike in demand coincides with the depletion of the fossil fuel resources, prompting the need for the development of renewable energy-storage systems.[1] Due to their extended cycle life, and high power and energy density, researchers have focused on second-generation lithium-ion batteries, fuel cells, and supercapacitors as viable and sustainable energy-storage options.[2,3] In this regard, batteries and supercapacitors (SCs) are both essential for storing renewable energy. Batteries have a high energy density due to redox processes, but their power density is restricted compared to supercapacitors.[4,5] Considering this, an extensive amount of research is being done to improve the energy density of SCs while maintaining their high-power properties. A major endeavor in this area is the development of hybrid energy-storage devices, with an aim to bridge the energy capacity gap between standard batteries and the power output of SCs. The hybrid supercapacitor (HSC) is one such invention that combines extraordinarily efficient battery-type electrode materials with capacitive grade materials.[6,7] In an HSC, faradaic reaction processes are enabled by the high energy potential of redox-active materials, which are generally used as positive electrodes (with high energy density), paired with carbonaceous materials that serve as negative electrodes (with high power density).[8,9] Redox-active metal oxides, owing to their high energy density and remarkable rate capabilities, are suitable choices for positive electrode materials.[5] In contrast, carbonaceous materials are frequently employed as electrodes in electric double-layer capacitors (EDLCs) due to their cost-effectiveness, resistance to high temperatures, high electrical conductivity, and excellent power density.[10,11]

In this regard metal–organic frameworks (MOFs) have emerged as a new class of crystalline materials, characterized by the coordination interactions between organic ligands and inorganic nodes, which are often metal ions or clusters with a high ability to store charge.[12] MOFs have a wide specific surface area, fully exposed active sites, and changeable structure due to their unusual inorganic and organic hybrid structure, and can be employed directly as electrode materials.[13] However, MOFs have several restrictions, such as low chemical stability and electrical conductivity,[14,15] that prevent them from reaching their full potential. However, their combination with

[a]*Renewable Energy Research Laboratory, Faculty of Engineering Sciences, Ghulam Ishaq Khan Institute of Engineering Sciences and Technology, Topi, 23640, Khyber Pakhtunkhwa, Pakistan. E-mail: zahir@giki.edu.pk*

[b]*Department of Chemistry, College of Science, King Saud University, Riyadh 11451, Saudi Arabia*

[c]*Department of Physics, Durham University, DH1 3LE, UK*

various functional materials, like metal oxides, can produce composites with the benefits of both parent materials while limiting their drawbacks.[16,17] Metal oxides with their unique properties have proven themselves as chemically appropriate and commercially feasible materials for energy technologies, such as batteries, fuel cells, water electrolysis, and small-molecules (*e.g.*, H_2O, CO_2, N_2) activation.[18–20] Lanthanides, having an electron configuration of $[Xe]4f^N$ (N = 0–14), are widely used in various applications due to the unique properties derived from their 4f electron configurations.[21–24] The majority of their chemical and physical properties are determined by the structure of their outer electronic layer.[25] Due to their redox activity, substantial bulk density, and high conductivity, lanthanides, notably rare earth metal oxides, are a major focus of research as an active electrode material for supercapacitors.[26,27]

In this regard, neodymium oxide (Nd_2O_3) is an important, highly redox active, and naturally abundant element.[28] Because of its strong structural qualities, resistance to corrosion, and high chemical stability it helps to improve the specific capacity and performance of the overall system by offering a long-lasting effectiveness and reliability in energy-storage devices by preventing deterioration and structural changes. Moreover, with a large surface area, copper cobalt–5-nitroisophthalic acid (CuCo(5-NIPA)) is ideal for cation intercalation/de-intercalation and electrochemical reactions during energy-storage activities, whereas the addition of metal oxides effectively increases the redox-active sites.[29,30] 5-Nitroisophthalic acid (5-NIPA) is a multifunctional ligand with a nitro group that has beneficial thermal as well as chemical stability and can also act as a hydrogen-bond acceptor to form hydrogen bonds. It also has a large number of coordination modes and the capacity to form clusters, which can serve as secondary building blocks in the formation of novel structural frameworks.[31] Porous coordination frameworks of 5-NIPA are observed due to their high coordination numbers as well as their unexpected and adaptive coordination behavior.[32]

Our study was aimed at merging the benefits of CuCo(5-NIPA) and Nd_2O_3 by making their composite with high surface areas, in which each component would preserve its uniqueness while imparting outstanding properties to the whole system.[33] The electron-withdrawing nitro group within 5-NIPA gave CuCo(5-NIPA) unique electrical characteristics. To further strengthen the energy-storage capacity of CuCo(5-NIPA), we utilized Nd_2O_3 to improve the stability and conductivity. The novelty of our work lies in the enhancement of the electrochemical properties of CuCo-based MOFs with a functionalized linker (5-NIPA) by integrating a rare earth metal oxide (Nd_2O_3). By utilizing the distinct advantages of each component, this study leveraged the synergistic interaction between Nd_2O_3 and the porous structure of CuCo(5-NIPA)–Nd_2O_3 to obtain higher electrochemical performance. Further, ample active sites for charge preservation and transport were provided by the MOF structure, while Nd_2O_3 improved the overall conductivity, which raised the redox activity and improved the energy-storage capacity. By working together, the potential of both materials was fully utilized, which could lead to further improvements in the functioning of energy-storage devices, such as batteries and supercapacitors. Complete electrochemical investigations were performed in a three-electrode assembly to compare the characteristics of CuCo(5-NIPA), Nd_2O_3, and CuCo(5-NIPA)–Nd_2O_3. Furthermore, CuCo(5-NIPA)–Nd_2O_3 was examined in a two-cell configuration to reveal the device performance. Following this, a semi-empirical approach was further employed to evaluate the capacitive as well as diffusive contributions using linear and quadratic models.

2. Experimental

2.1 Materials

CuCo(5-NIPA), Nd_2O_3, and their composite were examined *via* electrochemical analysis. *N*-Methyl-2-pyrrolidone (NMP), neodymium oxide, potassium hydroxide (KOH) pellets, activated carbon, acetylene black, DI water, and polyvinylidene fluoride (PVDF) were used in the electrochemical tests and were brought from Sigma Aldrich.

2.2 Synthesis

2.2.1 Synthesis of the copper-containing MOF. The Cu(5-NIPA) MOF was synthesized *via* sonication, as seen in Fig. 1, which required dissolving 0.25 mmol of nitro-isophthalic acid in 5 mL of DMF and DI water (30 : 70 v/v) in a beaker. Then, in 3 mL of the previously mentioned mixture, an equal quantity of copper acetate monohydrate was dissolved. Furthermore, HCl solution was added dropwise for combining the ligand and metal salt, which was then sonicated at an amplitude and frequency of 15 micron for 15 min, respectively, followed by temperature maintenance at 50 °C and slow evaporation. Resulting dark-blue needle-like crystals were obtained and were washed three times with DMF, DI water, acetone, and methanol before drying in the air.

2.2.2 Synthesis of the cobalt-containing MOF. For the synthesis of Co(5-NIPA) MOF, in a 5 mL mixture of DMF and DI water (30 : 70 v/v) 0.25 mmol of NIPA was dissolved. Following that, an equivalent amount of cobalt acetate monohydrate was mixed in 3 mL of the previously described mixture. The purification and synthesis processes for the cobalt-containing MOF were similar to those for the Cu(5-NIPA) MOF described above.

2.2.3 Synthesis of the CuCo–NIPA MOF. In two different beakers filled with 30 mL of acetic acid, 0.05 g of Cu(5-NIPA) and Co(5-NIPA) were dissolved. The mixtures of the two containers were mixed and stirred at 50 °C until a homogenous mixture was obtained. Following that for 20 min at room temperature, the mixture was subjected to 220 W ultrasonic radiation at a frequency of 23 kHz. Finally, the generated sediments were separated by centrifugation, and vacuum drying was carried out.

2.2.4 Synthesis and electrode preparation of CuCo–NIPA–Nd_2O_3. Considering the high porosity and conductivity of nickel foam, it was utilized as a current collector. Before being used to fabricate the electrode, the nickel foam was cleaned using ethanol, DI water, and 3 M HCl and then dried at 60 °C. Nd_2O_3 was used without any further purification and was purchased

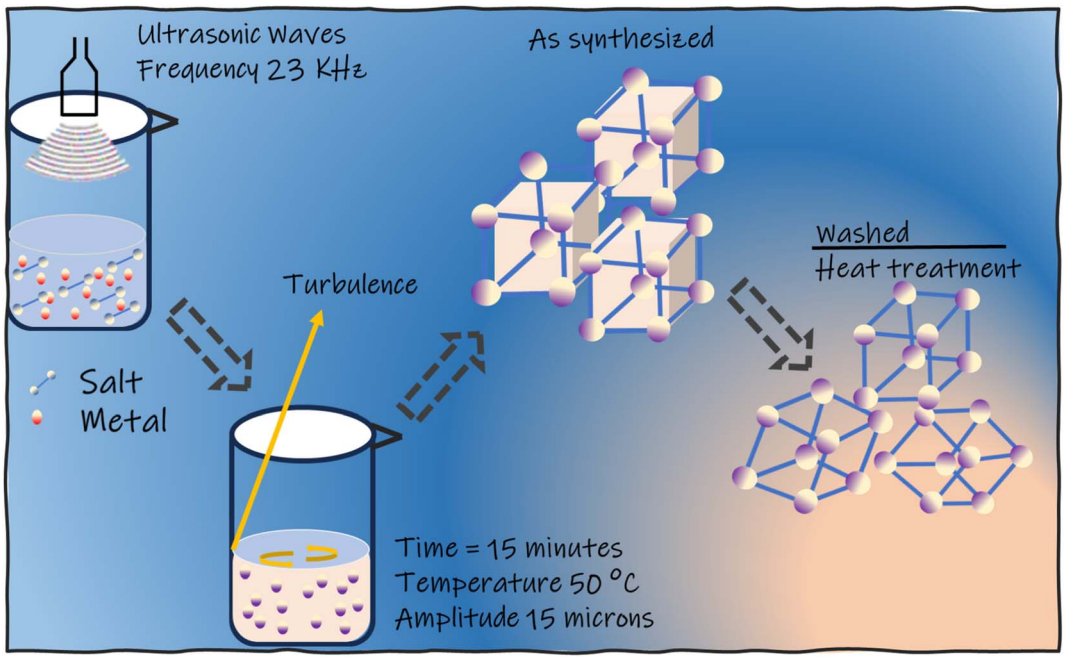

Fig. 1 Schematic synthesis of CuCo(5-NIPA) MOF *via* a sonochemical process.

from Sigma Aldrich. For synthesizing the CuCo(5-NIPA)–Nd_2O_3 composite electrode, a slurry was made by physical blending a mixture of 5% NMP, 40% Nd_2O_3, 40% CuCo(5-NIPA), 10% PVDF, and 10% carbon black acetylene. Before deposition, the mixture was completely blended overnight using a hot plate magnetic stirrer at 350 RPM. After that, the slurry was poured on the nickel foam and then heated in a furnace for an additional 3 h at 90 °C to complete the fabrication process.

2.2.5 Fabrication process of the hybrid device. Based on the results of the initial electrochemical testing in a half-cell mode, CuCo(5-NIPA)–Nd_2O_3 was used as a positive electrode to fabricate a hybrid device alongside activated carbon (AC) separated by a thin filter paper. For fabricating the negative electrode, the slurry consisted of 75% activated carbon, 15% acetylene black, and 10% PVDF dissolved in NMP solvent. The mixture was stirred overnight and then deposited on the nickel foam followed by oven drying at 80 °C for 4 h.

The mass loading on the electrode was calculated by mass balance according to eqn (1) below:

$$\frac{m_+}{m_-} = \frac{C_{s_-} \times \Delta V_-}{C_{s_+} \times \Delta V_+} \quad (1)$$

where the active masses, potential window, and specific capacities between the positive and negative electrodes are represented by m_+ and m_-, ΔV_+ and ΔV_-, and C_{s_+} and C_{s_-}. Thus, for the three-electrode system measurements, the mass of the active material was 4 mg, while for two-electrode assembly, the mass of the activated carbon was 7 mg.

2.3 Characterization

The structural and electrochemical characteristics of the synthesized CuCo(5-NIPA), Nd_2O_3, and CuCo(5-NIPA)–Nd_2O_3 electrodes were assessed through several characterizations. For examining the surface, morphological, and elemental features of the electrodes, X-ray diffraction (XRD), scanning electron microscopy (SEM), and energy dispersive X-ray analysis (EDX) were utilized. By utilizing a GAMRY Reference 3000 Potentiostat/Galvanostat, several techniques, including cyclic voltammetry (CV), galvanostatic charging and discharging (GCD), electrochemical impedance spectroscopy (EIS), and theoretical model fitting, were employed to assess the electrochemical performances of the electrodes. The synthesized electrode's performance was first evaluated in a three-cell configuration. Based on the results from the three-cell assembly, the top-performing sample was then assessed in a two-cell configuration for the battery–supercapacitor hybrid after being combined with activated carbon.

3. Results and discussion

3.1 Structural characterization

For analyzing the structural and morphological properties of CuCo(5-NIPA), Nd_2O_3, and their composite (CuCo(5-NIPA)–Nd_2O_3), XRD, EDX, and SEM were performed. Fig. 2(a)–(c) depict the XRD results, which revealed distinct peaks for CuCo(5-NIPA), Nd_2O_3, and their composite. The XRD patterns highlight the structural properties with the crystalline phases of the three samples. Moreover, the presence of peaks in the composite XRD pattern verified the existence of CuCo(5-NIPA) and Nd_2O_3.

Following this, for further assessing the elemental analysis and morphological features of the synthesized electrodes, EDX and SEM were utilized. The SEM micrographs along with the respective elemental compositions (EDX) for CuCo(5-NIPA),

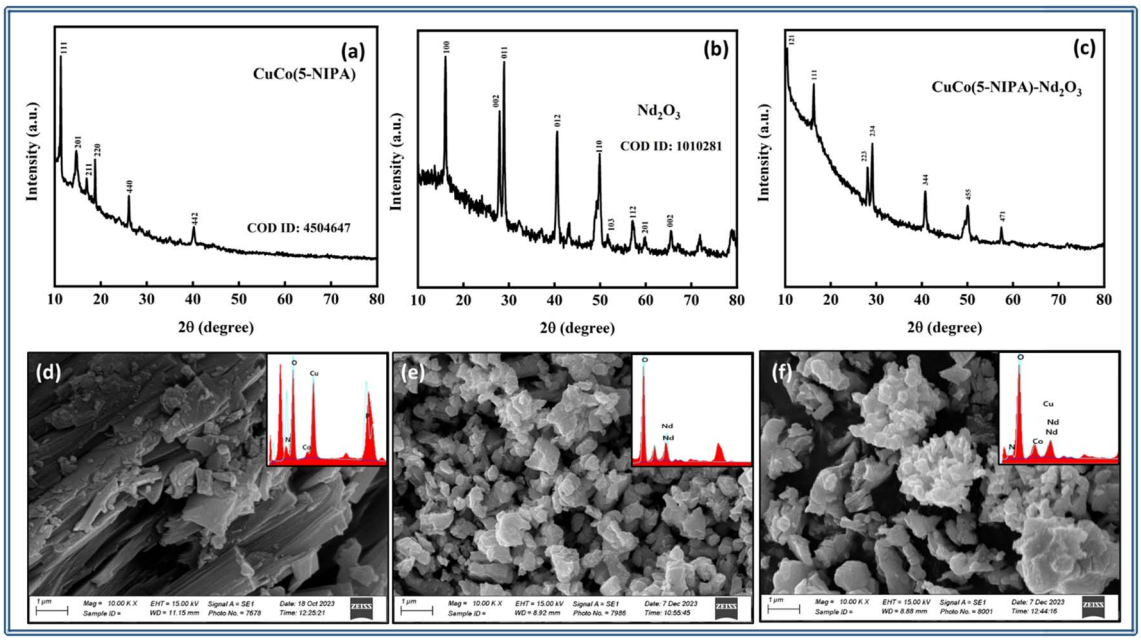

Fig. 2 X-Ray diffraction patterns of (a) CuCo(5-NIPA), (b) Nd_2O_3, and (c) CuCo(5-NIPA)–Nd_2O_3. Scanning electron microscopy images along with the Energy Dispersive X-ray analysis for (d) CuCo(5-NIPA), (e) Nd_2O_3, and (f) CuCo(5-NIPA)–Nd_2O_3.

Nd_2O_3, and CuCo(5-NIPA)–Nd_2O_3 are displayed in Fig. 2(d)–(f). From the micrographs, a flake-like morphology was noticed for CuCo(5-NIPA), which was attributed to their layered structure (a vital feature relevant to supercapacitor applications). A layered arrangement facilitates fast charge and discharge kinetics by accelerating the fundamental motion of ions in the electrode matrix, leading to an increase in ionic conductivity and rate capability for a material. Moreover, Nd_2O_3's crystalline nature could contribute to reducing the internal resistance and an increase in the energy-storage capacity through the effective conveyance, carrying, and conducting of charge. Furthermore, it could reduce structural degradation while promoting continuous ion adsorption and desorption, either of which could improve the supercapacitor's long-term robustness. Subsequently the composite CuCo(5-NIPA)–Nd_2O_3 showed that both Nd_2O_3 and CuCo(5-NIPA) coexisted. This offers more surface area and active sites by combining both their flaky and crystalline traits. These observations were further supported by electrochemical measurements in the half- and full-cells.

3.2 Half-cell assembly electrochemical characterization

3.2.1 Cyclic voltammetry analysis. One can identify reversible or irreversible redox reactions during CV monitoring by applying a potential sweep to the electrode. This approach contributes to the characterization of electrode materials by providing information on the electrode surface area, adsorbed species, and reaction kinetics. For monitoring the electrochemical behavior of the synthesized working electrodes in a three-cell assembly, Hg/HgO and platinum wire served as a reference and counter electrode. Fifteen CV cycles at 3 mV s^{-1} were initially employed for the testing and activation of the material. Fig. 3(a)–(c) display the voltammograms at various scan rates ranging from 3–50 mV s^{-1}. The presence of anodic and cathodic peaks in the voltammograms clearly shed light on the ongoing faradaic reactions between the electrode and electrolyte interface. These peaks indicated that the substances were electrochemically active and capable of reversible redox reactions. The CV profiles of each sample displayed tiny peaks at lower scan rates, indicating the presence of redox processes. These peaks and their associated currents increased at higher potential scan rates because of the rapid diffusion-controlled ion-transport kinetics of the basic electrolyte at the interface present between the electrode and electrolyte. Further, peak broadening was also observed in all the samples at higher scan rates, which resulted from the limited diffusion of the electroactive species as they did not have enough time to diffuse into the electrode material. In the meanwhile, providing glimpses of potential as battery-grade materials, the redox peak locations gradually moved, which might be because polarization arose because of the increase in scan rate. As the scan rate increased, the receding peaks indicated capacity restrictions caused by the reaction kinetics.

Moreover, the morphologies of the CV curves of CuCo(5-NIPA) remained unaltered even at a high scan rate of 50 mV s^{-1}, demonstrating its exceptional stability, while there was minimal change in the CV shape of Nd_2O_3, with one notable exception of an alteration in some peak positions. These voltammogram patterns show that the reactions were diffusion regulated, with the mass transport rate acting as the governing factor. This shows that the synthesized electrodes are capable of rapid and reversible faradaic reactions, highlighting their potential value in electrochemical applications. On the other hand, the CuCo(5-NIPA) and Nd_2O_3 composite's CV shape showed notable alterations, revealing the dominancy of electrochemical kinetics. This indicates that by adding one element to the other's matrix the

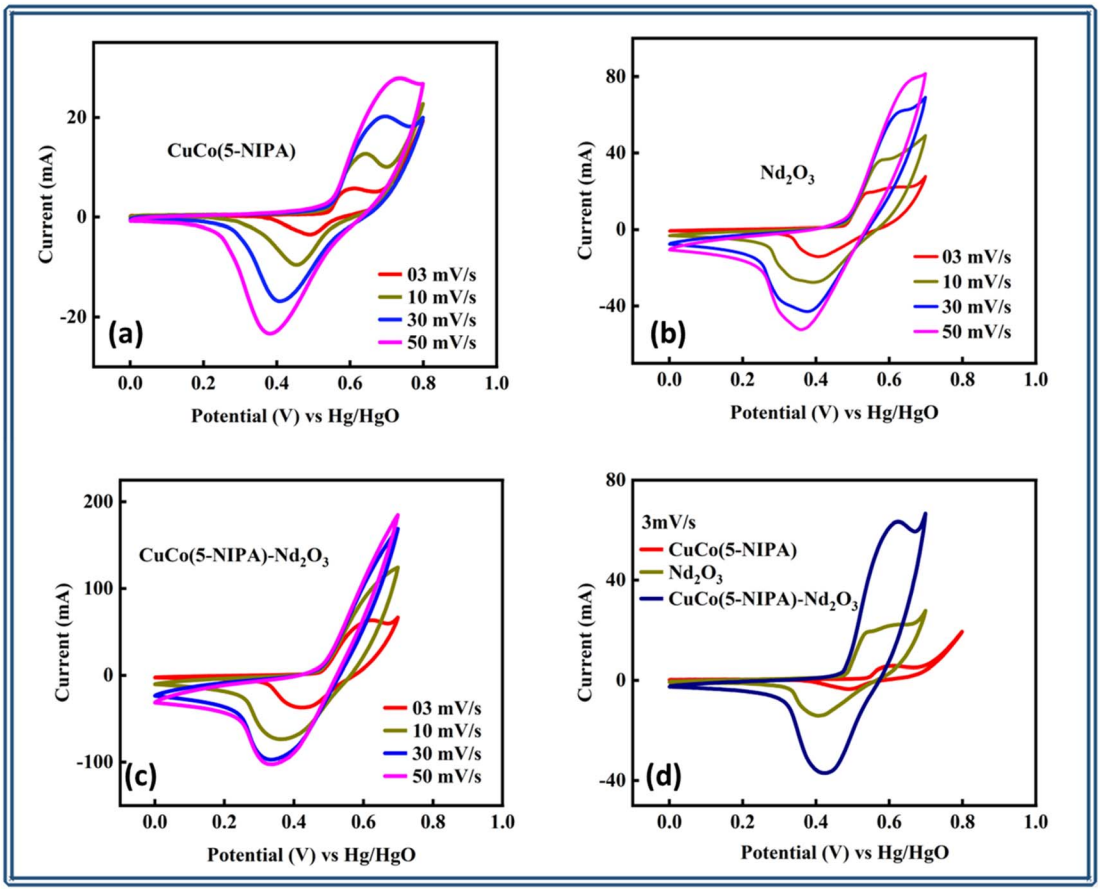

Fig. 3 Cyclic voltammograms of (a) CuCo(5-NIPA), (b) Nd_2O_3, and (c) CuCo(5-NIPA)–Nd_2O_3, (d) comparison of all three samples.

dynamics of the electrochemical process will change by providing new reaction avenues. Despite these modifications, the composite showed a larger integral area and peak current than the individual components, as shown by the comparison of the CV profiles of all electrodes at the lowest scan rate of 3 mV s^{-1} as illustrated in Fig. 3(d). CuCo(5-NIPA) most likely contributed to this improvement because of its large surface area and its abundance of redox-active sites derived from the cobalt and copper ions. Moreover, adding 5-NIPA could result in the emergence of novel functional groups or an upsurge in the quantity of charge-storage active sites that are easily accessible. The electrochemical performance of these sites was enhanced by the improved electron-transport mechanisms during charge/discharge cycles. Meanwhile, the electrochemically active Nd_2O_3 increased the number of redox-active centers in the composite. The presence of Nd_2O_3 facilitated the transition between Nd^{3+} and Nd^{4+} ions at the topmost layer, hence improving the total capacitance of the electrode material.

3.2.2 Galvanostatic charge–discharge (GCD) tests. In addition to CV, GCD is an important tool to evaluate the essential variables related to the electrochemical properties of materials, such as the specific capacity energy and power density, for analyzing the effectiveness of device. In GCD, voltage and current fluctuations are continuously applied to the electrodes, which are monitored over time, making it simpler to investigate the kinetics of charge transfer and ion diffusion in various electrode materials. Fig. 4(a)–(c) display the GCD profiles of CuCo(5-NIPA), Nd_2O_3, and CuCo(5-NIPA)–Nd_2O_3. A progressive rise and drop in voltage during charging and discharging, respectively, could be observed in these patterns. This means that the materials had a very consistent voltage profile, which is desirable for battery applications. Following a fixed potential zone, the nonlinear portion revealed the faradaic reaction on the most active locations of both electrodes, followed by ion desorption into the electrolyte. Furthermore, the GCD curves of all the samples exhibited a nonlinear behavior, with substantial humps in the charge–discharge curves, indicating the presence of faradaic reactions between the electrolyte ions and active material. Due to the limited ion movement to and from the electrode–electrolyte interface, the discharge duration was reduced with increased current density, leading to decreasing efficiency. Fig. 4(d) compares the GCD findings of all the samples and clearly shows that (CuCo(5-NIPA)–Nd_2O_3) had superior performance than the other two samples, as seen by its longer discharge time and slower voltage drop.

An electrode's charge-storage capacity may be evaluated by examining its CV curves, which are represented in terms of the specific capacity (C g^{-1}).

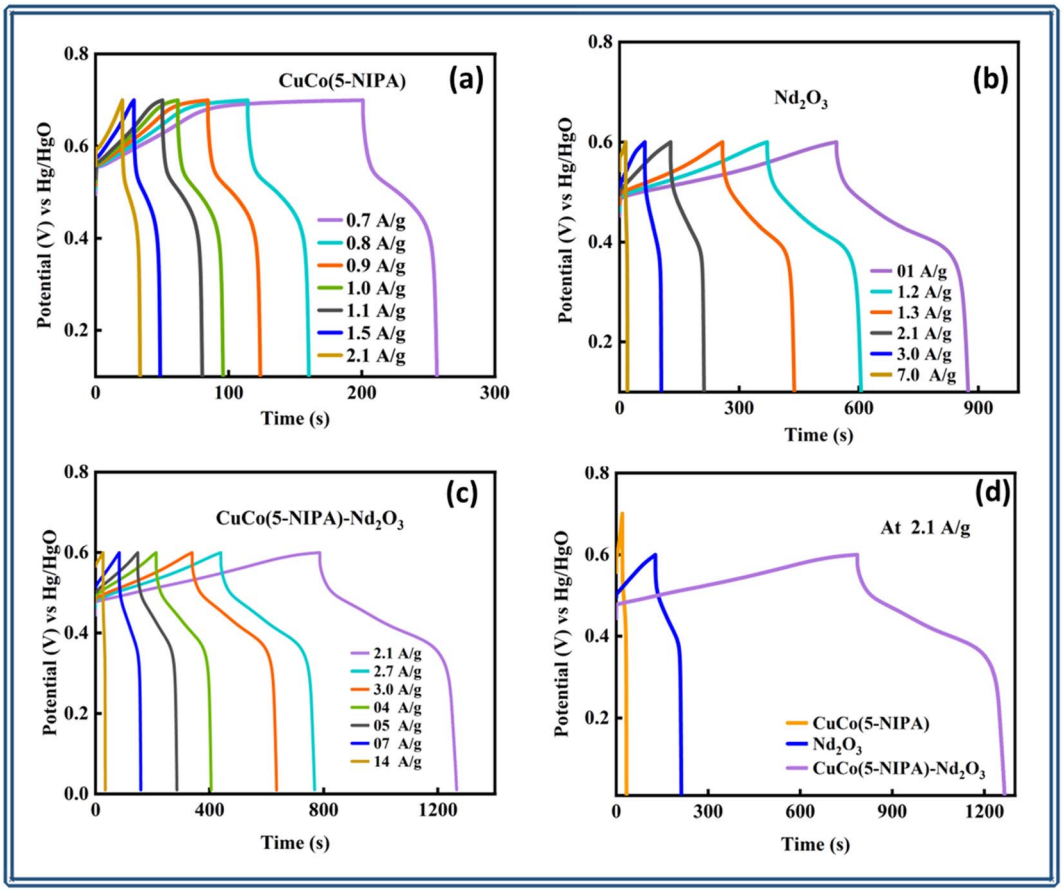

Fig. 4 Galvanostatic charge–discharge curves of (a) CuCo(5-NIPA), (b) Nd_2O_3, and (c) CuCo(5-NIPA)–Nd_2O_3, (d) comparison of the GCD curves of all three samples.

$$Q_s = \frac{1}{mv}\int_{V_i}^{V_f} I\,dV \quad (2)$$

The area under the CV curve is defined by the integral component, which determines the specific capacity, and is designated as Q_s in the equation above and represented in C g^{-1}. The scan rate and mass of the active material is denoted by "v" and "m", respectively. According to the prior correlation, a cyclic voltammetry (CV) curve with a larger active area is associated with a greater specific capacity at any given scan rate. Fig. 5(a) depicts the Q_s trend for all three samples in the half-cell assembly, where CuCo(5-NIPA), Nd_2O_3, and CuCo(5-NIPA)–Nd_2O_3 achieved Q_s values of 105, 467, and 1202 C g^{-1}, respectively, at a scan rate of 3 mV s^{-1}. It is critical to note that when the scan rates increase, the specific capacity falls, because the swift kinetics of the electrolyte ions restrict their contact time with the conducting electrode material. Additionally, eqn (3) was used to calculate the specific capacities (Q_s) of CuCo(5-NIPA), Nd_2O_3, and CuCo(5-NIPA)–Nd_2O_3 from the GCD analysis for all current densities.

$$Q_s = \frac{1}{m}(I \times t) \quad (3)$$

Here, I/m and t are the current density and time it takes for the sample to discharge, respectively.

Fig. 5(b) illustrates the Q_s for all samples determined by using the aforementioned relation at various current densities. The maximum Q_s values for CuCo(5-NIPA), Nd_2O_3, and CuCo(5-NIPA)–Nd_2O_3 were 45.6, 355.7, and 1012.2 C g^{-1}, respectively. At high current density values, Q_s had a diminishing tendency because of the quick kinetics of the electrolyte ions, which prevented them from successfully interacting with the active electrode material. The data demonstrate that the CuCo(5-NIPA)–Nd_2O_3 composite had exceptional rate capacity, which supports the electrode material's greater performance.

3.2.3 Electrochemical impedance spectroscopy analysis. Electrochemical impedance spectroscopy (EIS) measures the impedance response throughout a frequency range by delivering tiny amplitude alternating current pulses to electrodes. This method yields useful data on the kinetics of charge transfer, the behavior of the electrode/electrolyte interface, and the existence of any systemic diffusion limits. By fitting the experimental impedance spectra to equivalent circuit models, EIS data analysis allows for the quantitative evaluation of electrode performance and the discovery of any underlying mechanisms influencing the conductivity. EIS measurements were executed here across a frequency range of 0.1–100 kHz at

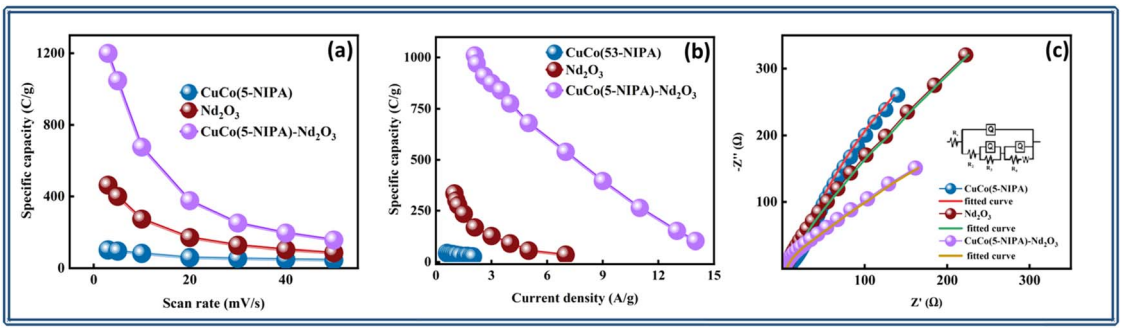

Fig. 5 (a) Specific capacities of CuCo(5-NIPA), Nd_2O_3, and CuCo(5-NIPA)–Nd_2O_3 through CV analysis. (b) Specific capacities of CuCo(5-NIPA), Nd_2O_3, and CuCo(5-NIPA)–Nd_2O_3 through GCD analysis. (c) Comparison of the electrochemical impedance spectroscopic curves for CuCo(5-NIPA), Nd_2O_3, and CuCo(5-NIPA)–Nd_2O_3 along with the fitted curves.

a constant amplitude of 10 mV. Fig. 5(c) displays the Nyquist plots along with the fitted curves for CuCo(5-NIPA), Nd_2O_3, and CuCo(5-NIPA)–Nd_2O_3. The study reported equivalent series resistance (ESR) values of 3.22, 1.2, and 0.3 Ω for CuCo(5-NIPA), Nd_2O_3, and CuCo(5-NIPA)–Nd_2O_3, respectively. The Nyquist plots demonstrated that the blended material's conductivity increased significantly. Notably, the absence of a semi-circle in the plots showed there was negligible resistance to charge transfer, although the linear trend at low frequencies suggested a capacitive behavior due to Warburg impedance (W_d), which indicates the accumulation of OH ions. The results emphasize the extent to which the CuCo(5-NIPA)–Nd_2O_3 combination is best for charge transfer. Moreover, CuCo(5-NIPA)–Nd_2O_3 has exceptional electrochemical properties as demonstrated by the EIS assessment. These results underline the composite's potential for a remarkable specific capacity because of its improved charge-transport capabilities and effective charge transfer across the electrode–electrolyte interface. Additionally, the obtained results validate the outcomes from the CV and GCD experiments. Thus, CuCo(5-NIPA) and Nd_2O_3 together consequently offer a promising avenue for supercapacitor technology development.

3.3 Electrochemical characterizations of a hybrid supercapacitor

It is evident from the electrochemical evaluation of all the samples in the three-cell configuration that the composite of MOF and the oxide performed better. Therefore, in an asymmetric design, the device was fabricated with the best-performing sample and activated carbon (AC) as positive and negative electrode materials, respectively. Fig. 6(a) displays a schematic representation of the device (CuCo–(5-NIPA)–Nd_2O_3//AC). The CV results for the CuCo(5-NIPA)–Nd_2O_3 and activated carbon electrodes are shown in Fig. 6(b), where the presence and absence of redox peaks, respectively, validate the capacitive and the battery-grade nature of the AC and CuCo(5-NIPA)/Nd_2O_3, respectively. The redox peaks made it easy to observe that the sample was capacitive and diffusion controlled. The device's CV curves for CuCo–(5-NIPA)–Nd_2O_3//AC at various scan rates ranging from 3 to 90 mV s^{-1} are depicted in Fig. 6(c), which highlights the device's stability and high capacity due to its ability to maintain its shape even at high scan rates. Additionally, the rectangular zone and spikes in the CV profiles confirmed the existence of both faradaic and non-faradaic processes.

The voltage window used in the CV measurements was repeated, and the GCD characterization was performed at different current density levels. The resulting charge–discharge curves are displayed in Fig. 6(d), where the non-linearity and humps in the GCD curves indicate both faradaic and non-faradaic charge-storage processes. The reversible electrochemical nature of the real device was illustrated by the regular symmetry of the curves. Notably, even at high scan rates, the GCD profiles of CuCo–(5-NIPA)–Nd_2O_3//AC remained unchanged, which emphasizes the device's exceptional rate capabilities. Furthermore, based on the GCD results, the specific capacities (Q_s) were estimated, and their trends are shown in Fig. 7(a). CuCo–(5-NIPA)–Nd_2O_3//AC showed a specific capacity (Q_s) of 467.5 C g^{-1}, which demonstrates the device's amazing rate capacity.

The actual device's energy density and power density were estimated by using the following equations:

$$P_s = \frac{E_s \times 3600}{t} \quad (4)$$

$$E_s = \frac{1}{7.2}(Q_s \times V) \quad (5)$$

where E_s is the energy density, V is the potential window, Q_s is the specific capacity, and P_s is the power density. CuCo–(5-NIPA)–Nd_2O_3//AC displayed a P_s of 4507 W kg^{-1} and an energy density E_s of 109.68 W h kg^{-1}, as depicted in Fig. 7(b), demonstrating the device's exceptional performance. Moreover, the cyclic performance of the composite was studied for a continuous 3500 charge–discharge cycles, as depicted in Fig. 7(c). After consecutive GCD cycles, the device retained 93.4% of its capacity along with a coulombic efficiency of 98.7%.

Furthermore, EIS tests were performed to evaluate the conductive properties of the CuCo–(5-NIPA)–Nd_2O_3//AC device. Fig. 7(d) depicts the Nyquist plot along with the fitted curve with an inset of the fitted circuit model $R(Q(R))$–$(R(RO))$. The device's

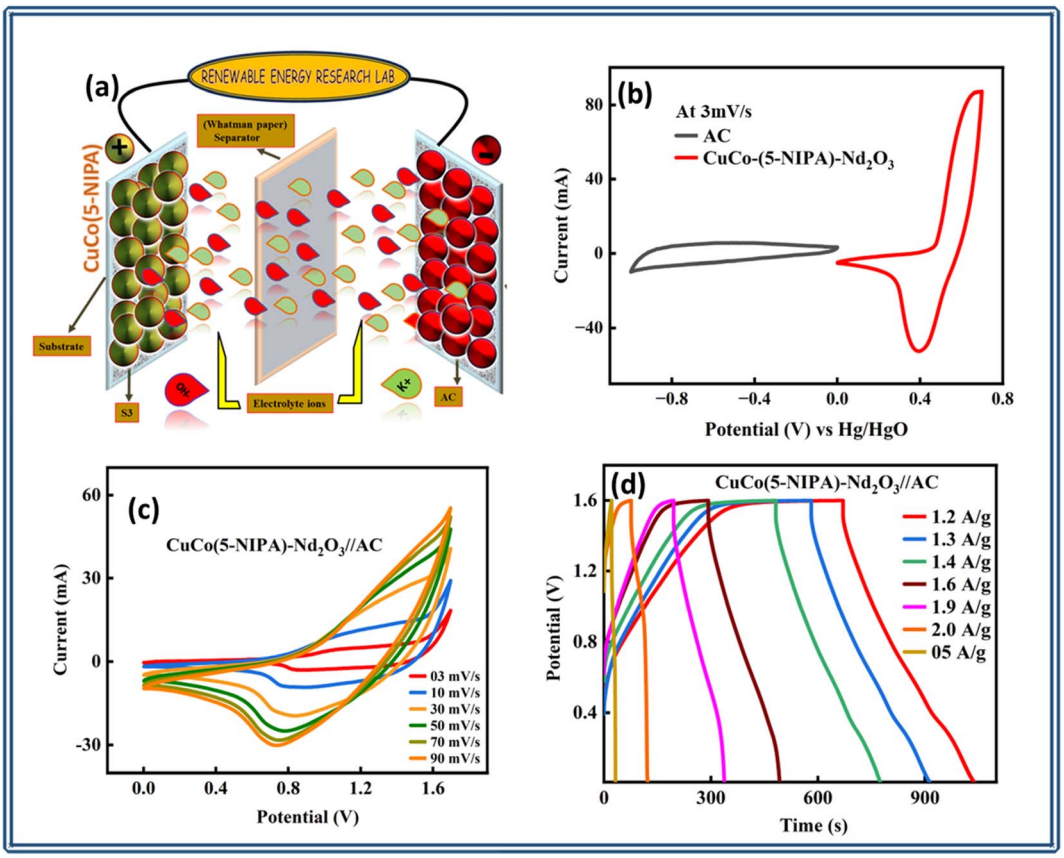

Fig. 6 (a) Schematic overview of the real device, (b) CV curves for activated carbon and CuCo(5-NIPA) at scan rate of 3 mV s^{-1} in three electrode asssembly, (c) CV curve for CuCo–(5-NIPA)–Nd_2O_3//AC. (d) GCD curves for CuCo–(5-NIPA)–Nd_2O_3//AC.

exceptional conductivity could be attributed to its low ESR value of 0.13 Ω.

3.3.1 Evaluation through semi-empirical models. To further investigate the electrochemical properties for the capacitive and diffusive behaviors, a simulated approach proposed by Dunn and his co-workers as the $\nu - \nu^{1/2}$ model (linear model) was contrasted with our more accurate quadratic model that has been published lately. The charge-storage mechanism in the hybrid device, owing to the presence of the positive (CuCo–(5-NIPA)–Nd_2O_3) and negative electrode material (AC), involved both faradaic (I_F) and non-faradaic (I_{NF}) reactions. This distinction arose from the ongoing internal mechanisms. SCs operate through non-faradaic processes, devoid of charge transfer, while leveraging the double-layer effect, where the current demonstrates a linear relationship with the scan rate. Conversely, batteries function *via* faradaic diffusion-limited redox reactions to generate energy. Consequently, we observed capacitive, pseudocapacitive, and diffusive effects, therefore:

$$I(\nu) = I_{NF} + I_F = k_1(\nu) + k_2\nu^{\frac{1}{2}} \quad (6)$$

where ν and k_1 and k_2 are the scan rate and regression coefficients, respectively. Capacitive and pseudocapacitive insertions are characterized by $k_1\nu$, whereas diffusion-controlled processes are indicated by $k_2\nu^{1/2}$. The contribution of the diffusive and capacitive processes to the overall charge-storage capacity of the device at different scan speeds (3, 50, and 90 mV s^{-1}) was demonstrated using linear and quadratic models. In both models, the experimental results confirmed that CuCo–(5-NIPA)–Nd_2O_3 exhibited dual characteristics of a battery and a capacitor, with the diffusive contribution marginally outweighing the capacitive contribution. Although the linear model made a reasonable attempt to adhere to the experimental pattern, as illustrated in Fig. 8(a)–(c), the fundamental assumption of linearity that underlies the model often does not hold across substantial portions of the data, *i.e.*, around peaks. Without this assumption, employing a linear model appears to be stretching its applicability. To overcome these limitations, we added a diffusive adjustment to the linear model, which expands it and produces a quadratic equation with respect to $\nu^{1/2}$. As a result:

$$I(\nu) = \beta_1(\nu) + \beta_2\nu^{\frac{1}{2}} + \beta_3\nu^{\frac{3}{2}} \quad (7)$$

where β_2 and β_3 are the regression parameters, which represent the faradaic processes, whereas the initial parameter β_1 encapsulates the combined impact of the double layer as well as pseudocapacitive effects. Using the quadratic model, at various scan speeds (3, 50, and 90 mV s^{-1}) as illustrated in Fig. 8(d)–(f), it could be seen that the contribution of the capacitive and diffusive processes matched well with the experimental data,

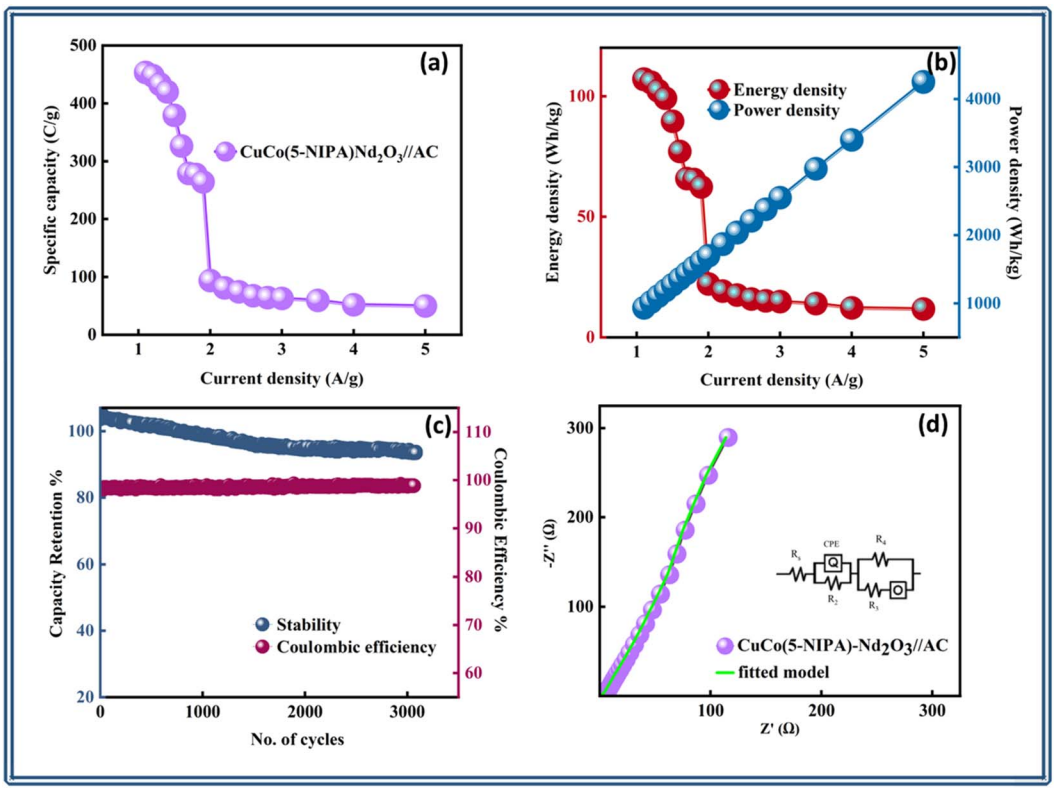

Fig. 7 (a) Specific capacity through GCD analysis, (b) energy and power density of CuCo–(5-NIPA)–Nd_2O_3//AC. (c) Capacity retention and coulombic efficiency with respect to the number of cycles, (d) electrochemical impedance spectroscopy plot for CuCo–(5-NIPA)–Nd_2O_3//AC with the fitted curve.

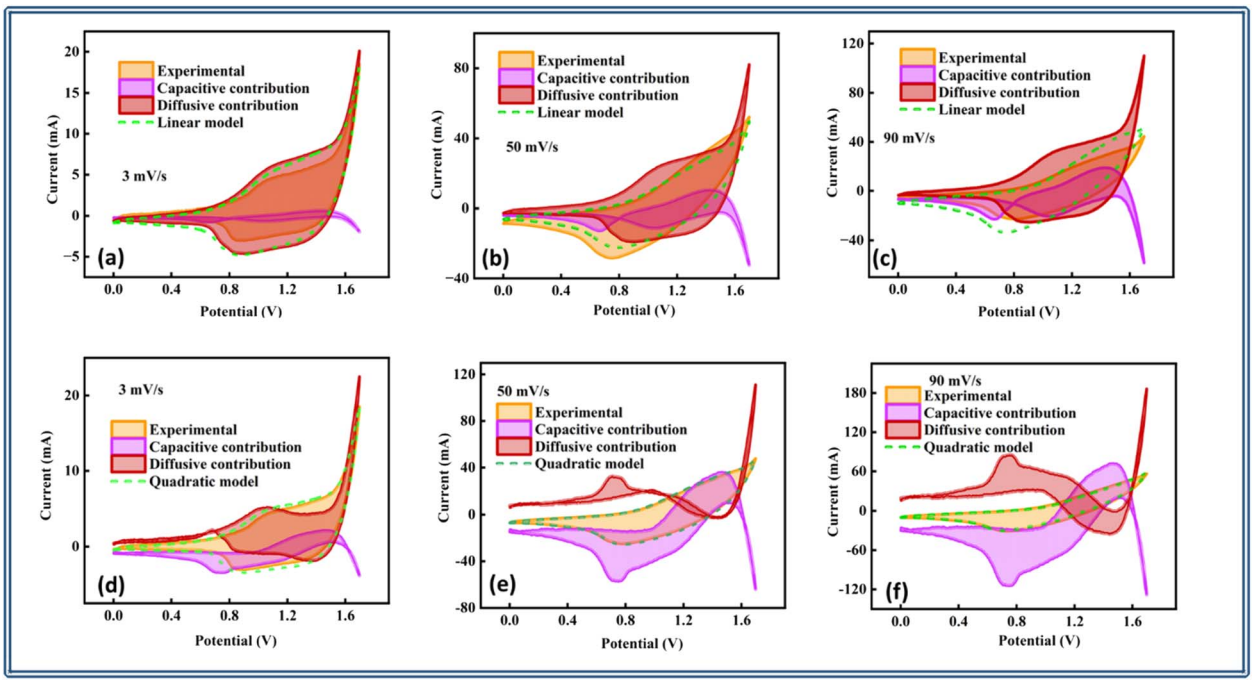

Fig. 8 Capacitive diffusive contributions at 3, 50, and 90 mV s^{-1} obtained through the (a)–(c) linear model and (d)–(f) quadratic model.

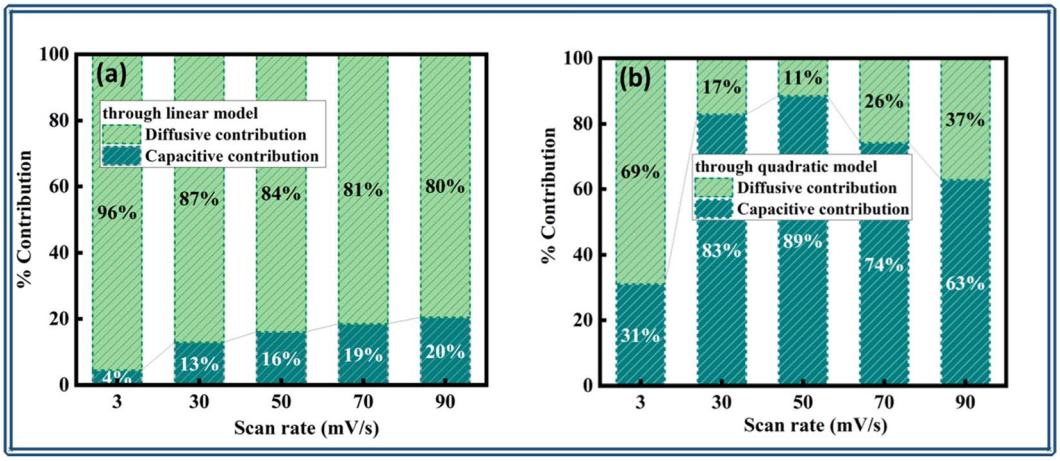

Fig. 9 Percentages of capacitive and diffusive contributions at various scan rates through the (a) linear model and (b) quadratic model.

which clearly shows that the quadratic model outperformed the linear model significantly. Additionally, in all these graphs for the linear and quadratic models, the combination of capacitive and diffusive contributions is shown by the linear and quadratic model fitting in Fig. 8(a)–(c) and (d)–(f), respectively. While both the models possessed error terms, the error in the linear model was more than in the quadratic model. Their sum increased the experimental data because of the limitation of the linear model, as shown in Fig. 8(a)–(c). As the error should be randomized, therefore we compared this with the quadratic model in which the fitting or (the sum of the capacitive and diffusive contributions) was matched more approximately with the experimental data, making it more accurate to investigate the capacitive and diffusive contributions of the device.

Furthermore, a bar plot was done that clearly illustrated the percentage fluctuation in the diffusive and capacitive components *versus* the matching scan speeds from both models, as shown in Fig. 9(a) and (b). The hybrid device's charge-storage chemistry demonstrated the involvement of both non-faradaic and faradaic (redox) processes due to the synergistic impact of the controlled diffusion and capacitive materials.

4. Conclusion

Concisely, for developing energy-storage devices, Nd_2O_3, CuCo(5-NIPA), and their composite, CuCo(5-NIPA)–Nd_2O_3, were electrochemically analyzed in half- and full-cell configurations. An in-depth study revealed the outstanding capabilities of the CuCo(5-NIPA)–Nd_2O_3 composite, with a specific capacity value of 1012.2 C g^{-1} at 2.1 A g^{-1}. This promising outcome prompted us to apply it in a hybrid supercapacitor device as the positive electrode material. This combination produced a specific capacity of 467.5 C g^{-1}. Furthermore, the real device exhibited exceptional energy-storage capacities, with a specific energy of 109.68 W h kg^{-1} and a specific power of 4507 W kg^{-1}. Afterwards, the capacitive and diffusive contributions were deconvoluted through linear and quadratic models. These findings highlight the enormous potential and step forward toward the development of self-supported electrode materials for innovative energy-storage applications that require high-performance solutions. This shows the prospects for developing enhanced energy-storage technologies utilizing these novel electrode materials.

Conflicts of interest

There are no conflicts to declare.

Acknowledgements

The work was supported by Researchers Supporting Project number (RSP2024R448), King Saud University, Riyadh, Saudi Arabia.

References

1 M. Mamizadeh, S. M. Masoudpanah, M. S. Bafghi and M. P. Dabir, *J. Energy Storage*, 2023, **63**, 106989.
2 Y. Lin, S. Su, Y. Cui, H. Dai, L. Lai and X. Zhu, *J. Mater. Sci.: Mater. Electron.*, 2023, **34**, 1308.
3 S. Yao and Y. Zhu, *Adv. Mater.*, 2015, **27**, 1480–1511.
4 Z. Wu, L. Li, J. m. Yan and X. b. Zhang, *Adv. Sci.*, 2017, **4**, 1600382.
5 T. Meng, Q.-Q. Xu, Z.-H. Wang, Y.-T. Li, Z.-M. Gao, X.-Y. Xing and T.-Z. Ren, *Electrochim. Acta*, 2015, **180**, 104–111.
6 F. Yu, C. Zhang, F. Wang, Y. Gu, P. Zhang, E. R. Waclawik, A. Du, K. K. Ostrikov and H. Wang, *Mater. Horiz.*, 2020, **7**, 495–503.
7 H. Shao, N. Padmanathan, D. McNulty, C. O'Dwyer and K. M. Razeeb, *ACS Appl. Energy Mater.*, 2018, **2**, 569–578.
8 J. Iqbal, A. Numan, S. Rafique, R. Jafer, S. Mohamad, K. Ramesh and S. Ramesh, *Electrochim. Acta*, 2018, **278**, 72–82.
9 J. Iqbal, A. Numan, R. Jafer, S. Bashir, A. Jilani, S. Mohammad, M. Khalid, K. Ramesh and S. Ramesh, *J. Alloys Compd.*, 2020, **821**, 153452.
10 S. Najib and E. Erdem, *Nanoscale Adv.*, 2019, **1**, 2817–2827.

11 R. S. Kate, S. A. Khalate and R. J. Deokate, *J. Alloys Compd.*, 2018, **734**, 89–111.
12 Y. Cui, B. Li, H. He, W. Zhou, B. Chen and G. Qian, *Accounts Chem. Res*, 2016, **49**, 483–493.
13 Z. Liu, F. Zheng, W. Xiong, X. Li, A. Yuan and H. Pang, *SmartMat*, 2021, **2**, 488–518.
14 L. Wang, Y. Han, X. Feng, J. Zhou, P. Qi and B. Wang, *Coord. Chem. Rev.*, 2016, **307**, 361–381.
15 H. Wang, Q.-L. Zhu, R. Zou and Q. Xu, *Chem*, 2017, **2**, 52–80.
16 S. Zheng, H. Xue and H. Pang, *Coord. Chem. Rev.*, 2018, **373**, 2–21.
17 F. Y. Yi, R. Zhang, H. Wang, L. F. Chen, L. Han, H. L. Jiang and Q. Xu, *Small Methods*, 2017, **1**, 1700187.
18 P. G. Bruce, B. Scrosati and J. M. Tarascon, *Angew. Chem., Int. Ed.*, 2008, **47**, 2930–2946.
19 D. G. Nocera, *Accounts Chem. Res*, 2012, **45**, 767–776.
20 R. Schlögl, *Angew. Chem., Int. Ed.*, 2011, **50**, 6424–6426.
21 M. A. Farrukh, K. M. Butt, A. Altaf and S. Khadim, *Silicon*, 2019, **11**, 2591–2598.
22 X. Li, F. Zhang and D. Zhao, *Nano Today*, 2013, **8**, 643–676.
23 Y. Zhang, Z. Song and F. Dong, *J. Lumin.*, 2012, **132**, 2462–2467.
24 J. Feng, R. Tang, G. Liu and T. Meng, *Chem. Eng. J.*, 2023, **452**, 139131.
25 J. Xu, H. Zou, H. Li, G. Li, S. Gan and G. Hong, *J. Alloys Compd.*, 2010, **490**, 552–556.
26 H. R. Naderi, M. R. Ganjali, A. S. Dezfuli and P. Norouzi, *RSC Adv.*, 2016, **6**, 51211–51220.
27 H. Li, S. X. Wang, Z. Huang, S. Zhang, Y. Li, L. Han and Z. Tan, *Polym. Adv. Technol.*, 2014, **25**, 1163–1168.
28 K. T. Kubra, R. Sharif, B. Patil, A. Javaid, S. Shahzadi, A. Salman, S. Siddique and G. Ali, *J. Alloys Compd.*, 2020, **815**, 152104.
29 J. Yang, F. Zhang, H. Lu, X. Hong, H. Jiang, Y. Wu and Y. Li, *Angew. Chem.*, 2015, **127**, 11039–11043.
30 J. Yu, C. Mu, B. Yan, X. Qin, C. Shen, H. Xue and H. Pang, *Mater. Horiz.*, 2017, **4**, 557–569.
31 S.-P. Chen, Y.-X. Ren, W.-T. Wang and S.-L. Gao, *Dalton Trans.*, 2010, **39**, 1552–1557.
32 M. Z. Iqbal, *J. Electroanal. Chem.*, 2020, **879**, 114812.
33 W.-w. Zhan, Q. Kuang, J.-z. Zhou, X.-j. Kong, Z.-x. Xie and L.-s. Zheng, *J. Am. Chem. Soc.*, 2013, **135**, 1926–1933.